JOURNAL OF THEORETICAL
AND APPLIED MECHANICS

ONLINE FIRST

# NUMERICAL SIMULATION STUDY ON CONTINUOUS SPAN VARIABLE CROSS-SECTION ARCHED ROOF

Qing ZHANG[1], Miao PENG[1*], Ji YAO[1], Yu ZHOU[2], Jianfeng HUANG[3]

[1] *Faculty of Civil Engineering and Mechanics, Kunming University of Science and Technology, Kunming 650500, China*
[2] *Yunnan Earthquake Engineering Research Center, Kunming 650228, China*
[3] *College of Civil Engineering and Architectural, Beibu Gulf University, Qinzhou 535011, China*
[*]corresponding author, *miaopeng@stu.kust.edu.cn*

Arched roofs are commonly utilized in various large-scale facilities for their remarkable stability and safety. With the advent of arched roofs featuring variable rise heights, there is a lack of research on wind pressure distribution and shape coefficients for these newer designs. This paper fills this gap by using the computational fluid dynamic (CFD) method on a continuous-span arched roof with different rise height, and valuable results have been obtained.

Results indicate that there will be significant positive pressure in the fence under different wind directions, while the maximum negative pressure and maximum velocity will occur in areas with significant changes in the cross-section of the fence structure. Except for the 90° wind direction, where the roof is primarily affected by positive pressure, the roof structure experiences a large area of negative pressure under other wind directions. The shape coefficients are negative and stable in wind directions of 0° and 180°. The coefficients under the 90° wind direction are all positive values, with slight drastic changes. Under wind directions of 45° and 135°, the variation of the shape coefficient is complex, with positive and negative values appearing. The influence of structural characteristics and size effects on the performance of the building roof is significant. The cantilevered structure of the roof can weaken the disturbance after the incoming flow impacts the building and the diffusion of the wake. Meanwhile, the changes in the size effect of the roof structure can lead to complex pressure distributions and shape coefficient values. The series of results indicate that the building's roof has good performance, with its wavy structure effectively reducing the pressure exerted by the incoming flow, ensuring safe operation. It is worth noting that there is always an area with a significant change in cross-sectional area in the fence structure under different wind directions, which tends to be subjected to greater negative pressure and requires more attention.

**Keywords:** wind pressure coefficient; shape coefficient; continuous variable cross-section arched roof; realizable $k$-$\varepsilon$ turbulence models; turbulent intensity.



## 1. Introduction

### 1.1. Research review

Large-span steel roof structures are particularly susceptible to wind forces. The impact of wind on the integrity and longevity of these roofs is a significant concern (Li *et al.*, 2007; Tian *et al.*, 2021). Arched roofs are known for their stability and safety under diverse wind conditions, although the complexity of calculating wind effects on their surfaces and their three-dimensional aspects is notable (Li *et al.*, 2010; Sun & Zhang, 2020; Tian *et al.*, 2021). Many scholars have conducted research on this type of roof.

Esfeh *et al.* (2021) numerically assessed the influence of wind direction on the ventilation capabilities of arched roofs with openings, highlighting the potential for reducing ventilation costs. Pagnini *et al.* (2022) used both numerical methods and wind tunnel tests to determine mean and peak wind coefficients on the inner and outer surfaces of arched canopies and suggested zoning approaches. Tian *et al.* (2021) proposed peak external wind pressure coefficients and more defined wind load zones for roof structures, informed by the updated wind load standards (JGJ/T 481-2019, 2020) and extensive wind tunnel data. Kim *et al.* (2019) measured wind pressure data for different roof styles and validated numerical simulations, finding the large eddy simulation (LES) particularly precise for predicting wind-related values for both single and multi-span arched roofs. Based on the EN 1991-1-4, Blackmore and Tsokri (2006) conducted wind tunnel studies to analyze wind coefficient patterns on arched roofs facing various wind directions and sizes, providing detailed regional categorizations and coefficient summaries to address gaps in existing guidelines, as illustrated in Fig. 1.

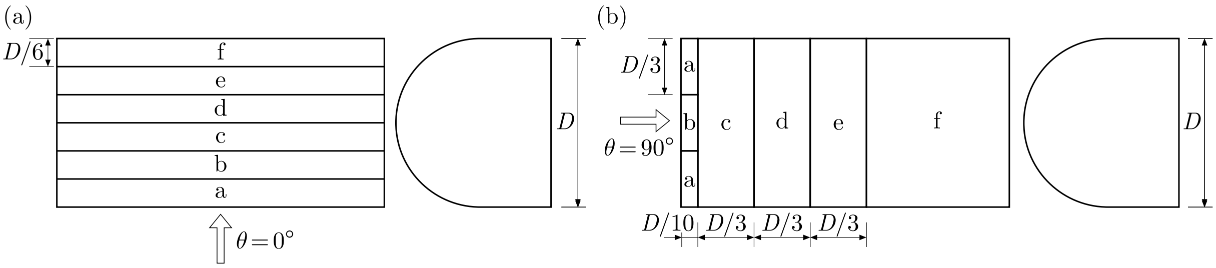


Fig. 1. Roof zoning of BRE wind tunnel test: (a) 0° wind direction; (b) 90° wind direction.

Li *et al.* (2006) explored the effects of different wind directions and conditions on the surface pressures of arched roofs with varying length-to-span ratios, noting the impact of the Reynolds number. Del Coz Díaz *et al.* (2013) conducted the computational fluid dynamics (CFD) analysis on large-span arched roof buildings under wind loading, evaluated roof wind pressure on arched roofs under wind loading, confirming that the results were in line with specifications and highlighting the need to consider localized suction effects in design. Paluch *et al.* (2003) studied the alterations in wind pressure and coefficients due to the addition of canopies to arched roofs, observing the differential effects of axial and vertical flows. Wang *et al.* (2023) numerically assessed the wind pressure coefficient variations in large-span industrial facilities, emphasizing the role of wind direction and terrain roughness.

### 1.2. Study purpose

The above researches have thoroughly explored the wind pressure dynamics of arched roofs. Recently, there has been a growing trend in the construction of large-span athletic facilities that feature arched roofs with varying cross-sections, a design that harmoniously blends aesthetic appeal with functional utility. Despite this, existing international standards (JGJ/T 481-2019, 2020) have not adequately addressed the study of wind pressure coefficients or form factors for these types of roofs, indicating a gap in the research for such coverings.

In response, this paper employs CFD to examine the wind field characteristics of a continuous span arched roof with a variable cross-section (discussed in Subsection 2.1). It analyzes the flow field dynamics, wind pressure, and form factor distributions across the roof under various wind orientations.

## 2. Method, setting and verification

### 2.1. Geometry and computational domain

Currently, numerical simulations are increasingly being used to examine the performance and flow patterns of building structures under wind action. This method can conduct the comprehensive analysis and evaluation of the building prior to construction, which can save costs.

The parameters for the numerical simulation are derived from a large venue located in Dali, Yunnan Province, China with the length, width and height parameters shown in Table 1. As shown in Fig. 2b, the building roof is symmetrical on both sides, with a shape similar to the wings of a butterfly and a narrow front (60.7 m) and wide back (89 m) shape. The structure of the roof is like rolling waves, undulating up and down (hereinafter referred to as a wavy roof), mainly composed of 4 peaks and 3 troughs as shown in Fig. 2e. As shown in Fig. 2c, it can be seen that the height of the peak is constantly changing. Furthermore, it is worth noting that the roof of the building is larger than the fence structure, which results in some areas of the wave peaks becoming cantilever structure.

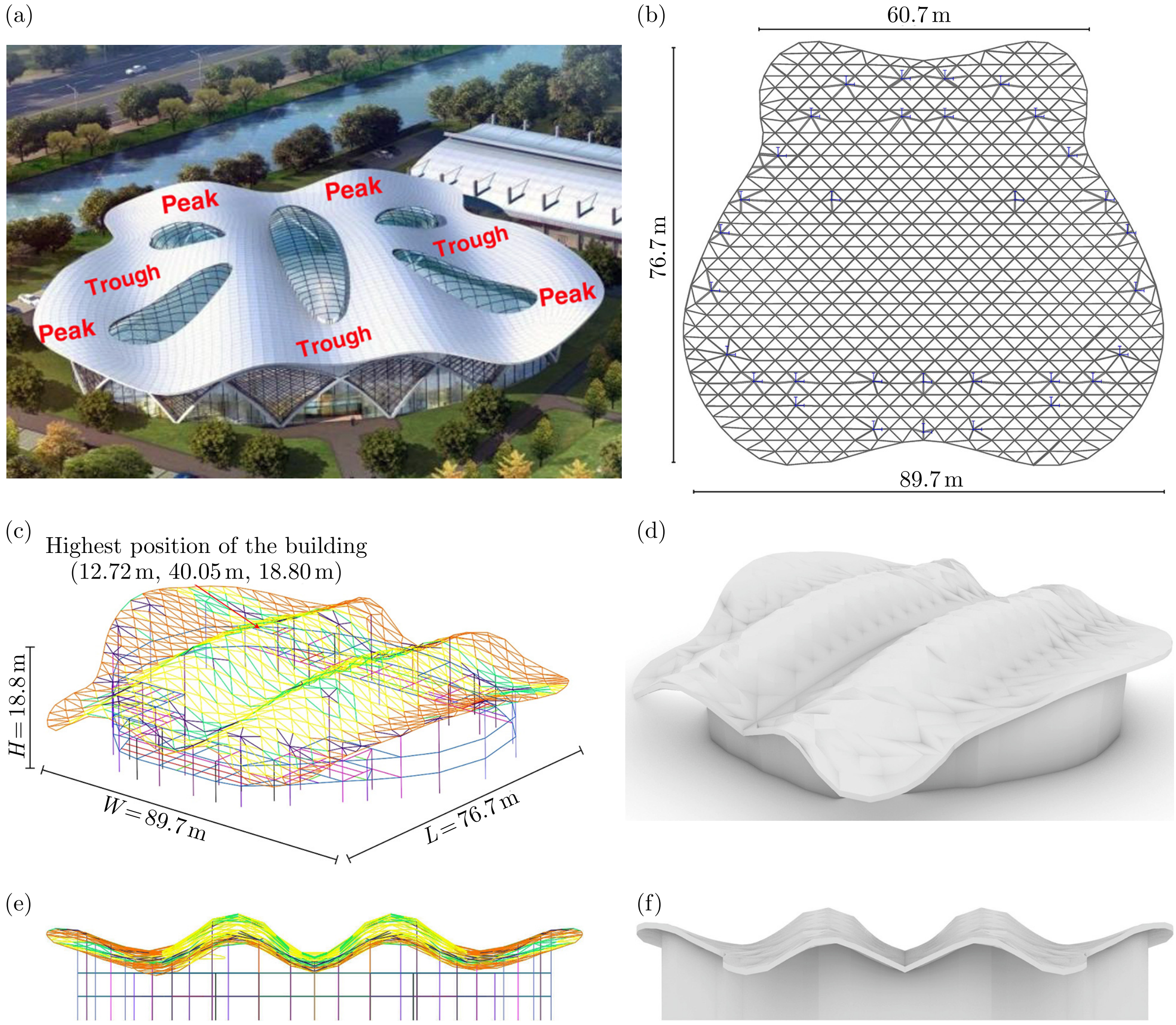


Fig. 2. Rendering, model diagram and dimensions.

Table 1. Model size.

| Parameters | Length $L$ [m] | Width $W$ [m] | Height $H$ [m] |
|---|---|---|---|
| Size | 76.7 | 89.7 | 18.8 |

It is crucial to ensure that the analysis model remains unaffected by the flow field's inlet and outlet boundaries, while also maintaining similarity between the numerical model and the real-world counterpart. Additionally, it is essential to mitigate the impact of blockage effects, which is achieved through the following equation:

$$\delta = A/A_0, \tag{2.1}$$

where $A$ and $A_0$ denote the areas of the model and the computational domain, respectively. The ratio is known as the blockage ratio, should be less than 5 %. Furthermore, it is necessary to ensure an adequate distance between the model and the computational boundaries. The height of the computational domain should exceed the model's height by at least 2 to 2.5 times, and the width should be at least 6 times greater than the model's width. The distance separating the inlet and outlet of the computational domain should be a minimum of 5 times the height of the model (Esfeh *et al.*, 2021; Wang *et al.*, 2023; Zhang *et al.*, 2021).

Building on the preceding analysis, the computational domain is established with a height of $5H$ (94 m), width to $6.2W$ (556.14 m) and length to 348.5 m. The model is $5H$ from the inlet, $10H$ from the outlet, which ensure the full development of the flow field. Based on the above settings, the blockage rate meets the requirements, as shown in Table 2. In addition, a body of influence has been set up near the model to encrypt the mesh near the model in the Subsection 2.3. The configuration of the computational domain is depicted in Fig. 3.

Table 2. Blockage rate of different wind directions.

| Wind directions | $A$ [m$^2$] | $A_0$ [m$^2$] | Blockage rate [%] |
|---|---|---|---|
| 0°/180° | 1686.36 | 52277.16 | 3.23 |
| 45°/135° | 2218.80 | 62207.65 | 3.57 |
| 90° | 1441.96 | 33717.80 | 4.28 |

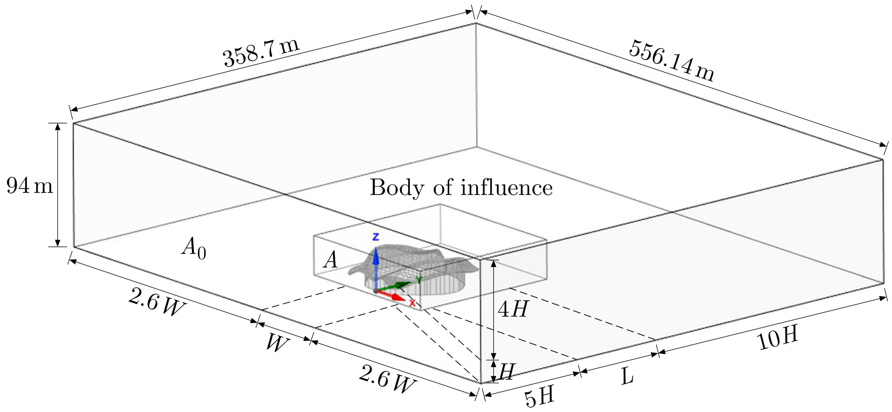


Fig. 3. Computational domain.

## 2.2. Turbulence model and boundary conditions

The Reynolds number (Re, a ratio of inertial force to viscous force) is an important parameter for determining the fluid state near buildings. The Reynolds number is determined by:

$$\mathrm{Re} = \frac{UL}{v}, \tag{2.2}$$

where $U$ is the wind of building height, which is 8 m/s, $v$ is the kinematic viscosity of the wind, which is $1.48 \times 10^{-5}$ m$^2$/s at standard conditions, $L$ is the characteristic length. The calculated Re is $5.4 \times 10^5$, indicating that the flow field near a building roof is in a turbulent state.

To efficiently simulate turbulent flows, different turbulence modeling approaches have been developed, including direct numerical simulation (DNS), LES, and the Reynolds-averaged Navier–Stokes (RANS) methods. Among these, DNS and LES are computationally intensive and require significant resources, limiting their widespread use in engineering applications. The RANS method is the most commonly used in practice due to its ability to produce satisfactory results with reasonable computational efficiency under appropriate parameter selections (del Coz Díaz *et al.*, 2013; Meng *et al.*, 2018; Zhang *et al.*, 2021).

The instantaneous equations are given as follows:

$$\frac{\partial \rho}{\partial t} + \nabla \cdot [\rho(\overline{v} - v_r)] = 0, \tag{2.3}$$

$$\frac{\partial}{\partial t}(\rho\overline{v}) + \nabla \cdot [\rho\overline{v}(\overline{v} - v_r)] = -\nabla \cdot \overline{p}I + \nabla \cdot \left(T - \rho\overline{v'v'}\right) + f_b, \tag{2.4}$$

where $\rho$ is the density of air, which is taken as $1.225\,\mathrm{kg/m^3}$.

The realizable $k$-$\varepsilon$ turbulence model is known for its effectiveness in simulating fluid flows in numerical simulations, particularly in scenarios involving rapid strain, streamline curvature, flow separation, reattachment, and recirculation. Consequently, this turbulence model was selected for the numerical simulation (Meng *et al.*, 2018; Zhang *et al.*, 2021). The governing equations for this model are presented in Eqs. (2.5) and (2.6):

– $k$-equation:

$$\frac{\partial(\rho k)}{\partial t} + \frac{\partial}{\partial x_k}(\rho k u_k) = \frac{\partial}{\partial x_k}\left[\left(\mu + \frac{\mu_t}{\sigma_k}\right)\frac{\partial k}{\partial x_k}\right] + G_k + G_b - \rho\varepsilon - Y_M + S_k, \tag{2.5}$$

– $\varepsilon$-equation:

$$\begin{aligned}\frac{\partial(\rho\varepsilon)}{\partial t} + \frac{\partial(\rho\varepsilon u_k)}{\partial x_k} = \frac{\partial}{\partial x_k}\left[\left(\mu + \frac{\mu_t}{\sigma_\varepsilon}\right)\frac{\partial \varepsilon}{\partial x_k}\right] + \rho C_1 S\varepsilon \\ - \rho C_2\frac{\varepsilon^2}{k + \sqrt{\nu\varepsilon}} + C_{1\varepsilon}\frac{\varepsilon}{k}C_{3\varepsilon}G_b + S_\varepsilon,\end{aligned} \tag{2.6}$$

$$\frac{U(z)}{U_H} = \left(\frac{z}{z_H}\right)^{\alpha}. \tag{2.7}$$

The characteristics of the incoming flow are of significant importance. Considering the specific circumstances, national standards, and relevant references, this study establishes the ground roughness coefficient as category IV, in accordance with GB 50009-2012 (2012). To represent the wind speed profile Eq. (2.7) (refer to Fig. 4a) is utilized, taking into account the inflow conditions of the atmospheric boundary layer wind. $U(z)$ denotes the wind speed at height $z$, $U_H$ is the wind speed at the building height of $z_H = 18.8\,\mathrm{m}$, set as $8\,\mathrm{m/s}$, and $\alpha$ represents the wind profile coefficient, set as 0.27.

Turbulent intensity $I$ serves as a crucial parameter that influences the dynamics of wind flow during separation events and is incorporated into numerical simulations through Eq. (2.8) (refer to Fig. 4b). In this context, $z_G$ means gradient wind height, set as $550\,\mathrm{m}$, and the turbulence intensity at the building height of 18.8 m is specified as 0.295:

$$I = 0.1\left(\frac{z}{z_G}\right)^{-\alpha-0.05}. \tag{2.8}$$

Turbulent kinetic energy $k$ and turbulent dissipation rate $\varepsilon$ are calculated using Eqs. (2.9) and (2.10), as illustrated in Figs. 4c and 4d, respectively. Notably, $a$ in Eq. (2.9) is a constant that depends on the standard deviations of turbulent fluctuations and is assigned a value of 1.0 for this numerical simulation:

$$k(z) = a\left(I(z) \cdot U(z)\right)^2, \tag{2.9}$$

$$\varepsilon = \frac{k^{1.5} \cdot C_u^2}{0.07L_u}. \tag{2.10}$$

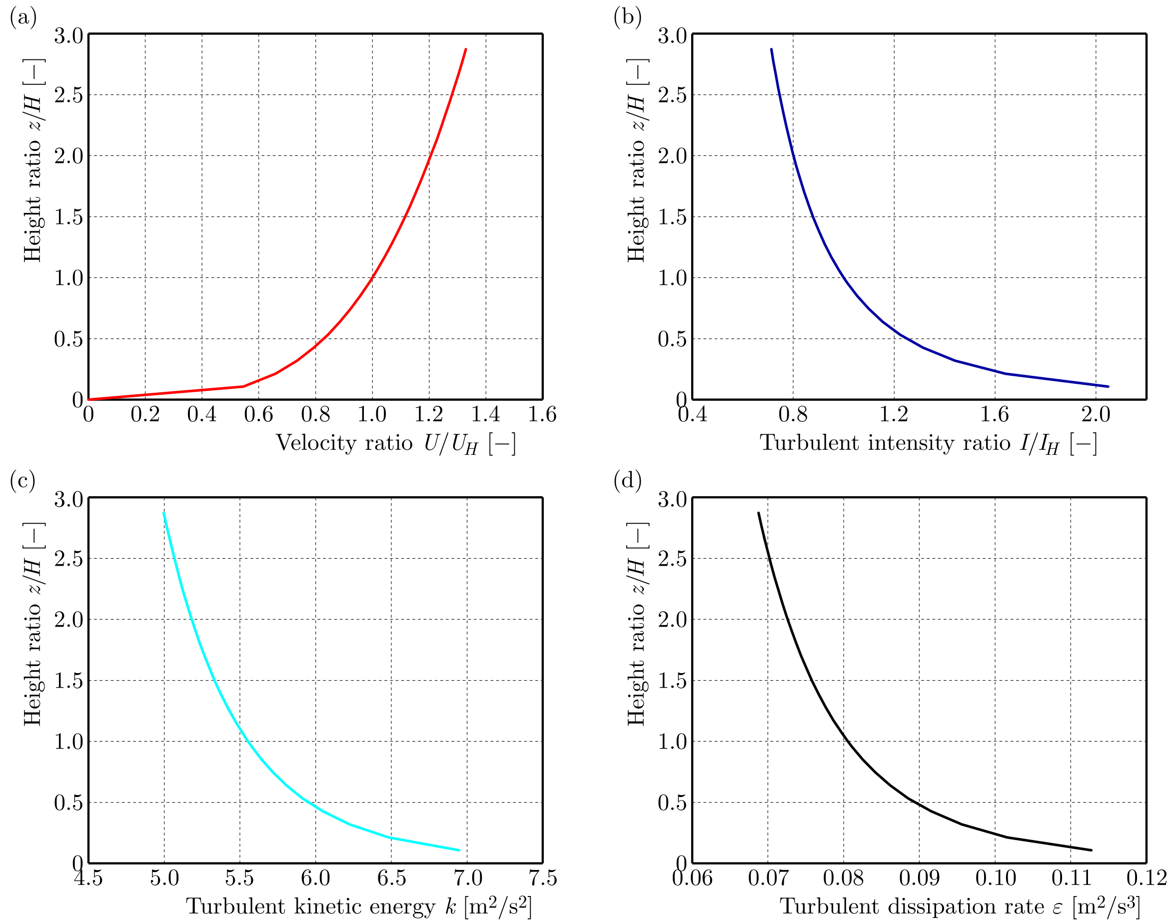


Fig. 4. Profiles of: (a) wind speed; (b) turbulent intensity; (c) turbulent kinetic energy, and (d) turbulence dissipation rate. Note: $H$ signifies the height of the model, and $I_H$ denotes the turbulence intensity at the building height.

The turbulence dissipation rate equation involves a characteristic length of the computational domain, $L_u$ is the characteristic length of a computational domain, set as 18.8 m. $C_u$ is an empirical constant, set as 0.09.

The boundary conditions are defined as depicted in Fig. 5. As previously discussed, the velocity-inlet is characterized by an exponential wind speed profile, the outlet boundary is designated as a pressure-outlet, and the surfaces of the building and the computational domain are treated as frictionless-walls. The simulation employs the SIMPLEC algorithm and a second-order upwind scheme for discretizing momentum, turbulent kinetic energy, and turbulent dissipation rate (del Coz Díaz *et al.*, 2013; Meng *et al.*, 2018). Convergence of the simulation reaches is

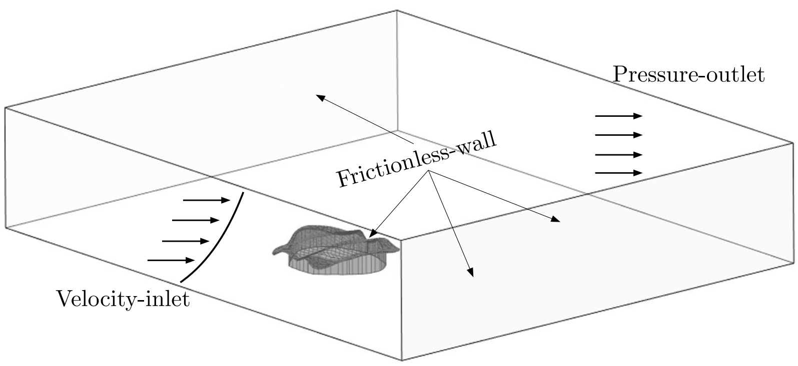


Fig. 5. Boundary conditions.

assumed when the residual of continuity, the momentum of $x$, $y$, $z$, $k$, $\varepsilon$ equations decrease below $10^{-6}$.

### 2.3. Grid division and verification

The flow conditions on the model roof are intricate and necessitate a refined mesh. Consequently, the rate of mesh growth near the model's wall is adjusted to 1.15 times to maintain a seamless transition between the mesh and the model. Furthermore, the grid height of the initial layer is meticulously chosen to guarantee that the value of $y^+$ is less than 1 (Esfeh *et al.*, 2021; Meng *et al.*, 2018; Zhang *et al.*, 2021). The grid layout is illustrated in Fig. 6a.

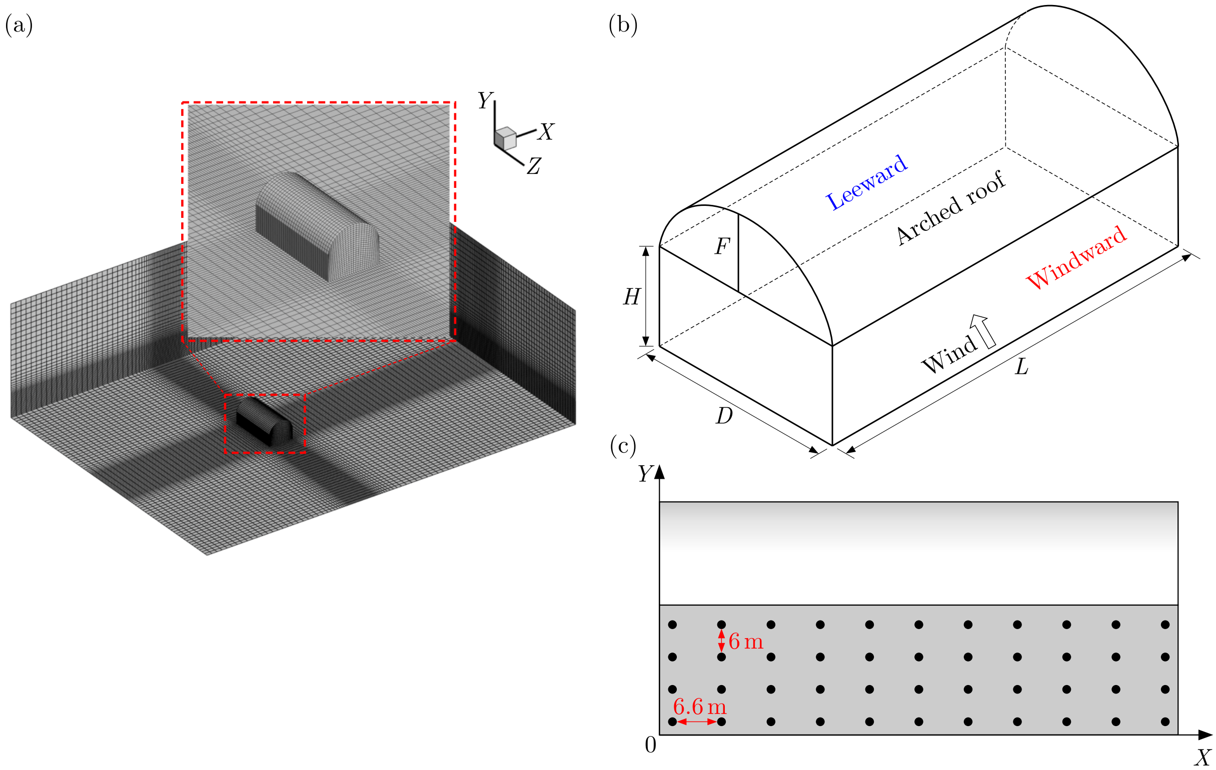


Fig. 6. (a) Grid partitioning and refinement; (b) standardized arched roof model; (c) setting of measuring points.

The codes do not provide the standard values for the shape coefficient of such roofs. So, we selected an arched roof in the codes (JGJ/T 481-2019, 2020) that is similar to the research object of this article. As shown in Fig. 6b, the roof parameters are $L/D = 2$, $F/D = 0.25$, calculating the coefficients on the windward and leeward surfaces and compare them with the standard values for verification based on 5 different grids. Also, the 5 grid size settings are shown in Table 3.

Table 3. Dimensions of 5 grids.

| Mesh type | Mesh number | Minimum size | Minimum volume [m$^3$] |
|---|---|---|---|
| Grid-1 | 15543 | $0.07235L$ | 38.05 |
| Grid-2 | 49392 | $0.05605L$ | 10.76 |
| Grid-3 | 128478 | $0.03620L$ | 3.79 |
| Grid-4 | 247848 | $0.02630L$ | 1.55 |
| Grid-5 | 357048 | $0.01975L$ | 0.74 |

The operation is as follows, set measurement points on the windward and leeward sides, as shown in the Fig. 6c. Set a measuring point at an interval of 6.6 m in the $X$-direction and a measuring point at an interval of 6 m in the $Y$-direction. There is a total of 88 measuring points. Wind pressure coefficients are calculated through Eq. (2.11). And use Eq. (2.12) to calculate the shape coefficient:

$$C_{pi} = \frac{P_i - P_\infty}{\frac{1}{2}\rho U_\infty^2}, \tag{2.11}$$

$$\mu_{si} = C_{pi}\left(\frac{z_H}{z_i}\right)^{2a}, \tag{2.12}$$

$$\mu_s = \frac{\sum_{i=1}^{n} \mu_{si} A_i}{\sum_{i=1}^{n} A_i}, \tag{2.13}$$

$$\gamma = \frac{|\mu_s - \mu_{s,\text{standard}}|}{\mu_{s,\text{standard}}}, \tag{2.14}$$

where $C_{pi}$ is the wind pressure coefficient of a specific point $i$, $P_i$ represents the wind pressure, $P_\infty$ is the static pressure at the reference height, $U_\infty$ is wind speed at the reference height, $\mu_{si}$ is the local shape coefficient of measuring points, and $\mu_s$ is the mean shape coefficient, $\mu_{s,\text{standard}}$ is the standard values from codes, $z_H$ and $z_i$ is the height of the building height and measuring points, $A_i$ is the area of measuring points.

As indicated in Table 4, it is evident that the $\mu_s$ on both the windward and leeward sides of the roof decrease progressively and converge towards the standard values as the grid is refined. Figure 7a illustrates the discrepancy between the CFD results and the codes (JGJ/T 481-2019, 2020).

Table 4. Results under 5 different grids.

| $\mu_s$ | Grid number | | | | |
|---|---|---|---|---|---|
| | Grid-1 | Grid-2 | Grid-3 | Grid-4 | Grid-5 |
| Windward side | 1.52 | 1.06 | 0.85 | 0.74 | 0.74 |
| Standard | +0.80 | | | | |
| Leeward side | −0.55 | −0.46 | −0.36 | −0.42 | −0.37 |
| Standard | -0.40 | | | | |

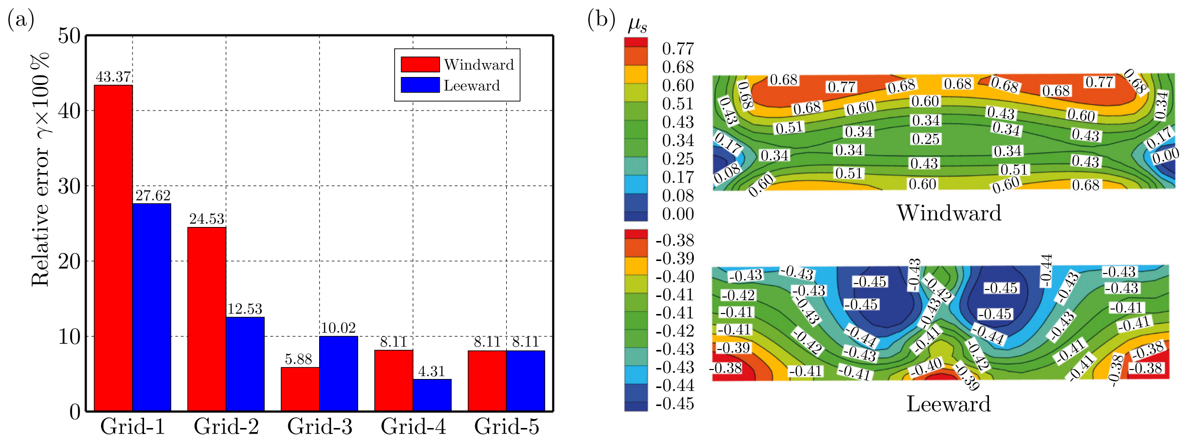


Fig. 7. (a) Deviation of shape coefficient under 5 grid models; (b) local shape coefficient of windward and leeward under Grid-4.

As the number of grid cells rises, it becomes clear that the absolute deviation between the calculated results and the actual values diminishes. The results from Grid-4 and Grid-5 exhibit a trend towards stability, with the absolute deviation dropping below 10 %. Given that Grid-4 has a lower grid count and demands fewer computational resources, it is selected as the standard for the grid division in the subsequent analysis.

### 2.4. CFD verification

Select the same model as in Subsection 2.3 and use the same method to calculate the shape coefficients of the roof to verify the feasibility of CFD method. Figure 8 shows the wind zone method and measurement points set on the roof. The mean shape coefficients of the 3 zones were obtained by calculating the local shape coefficient. The results are shown in Fig. 9.

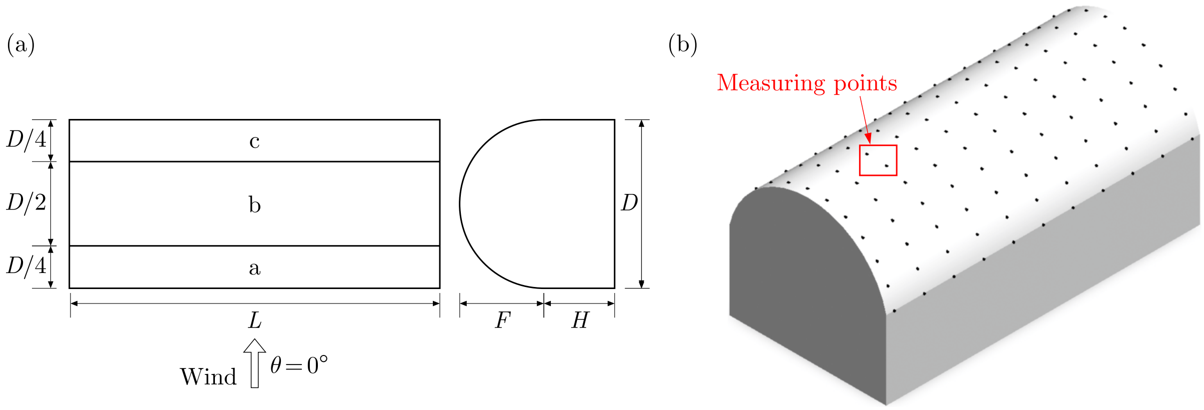


Fig. 8. (a) Standardized roof zoning; (b) measuring points settings.

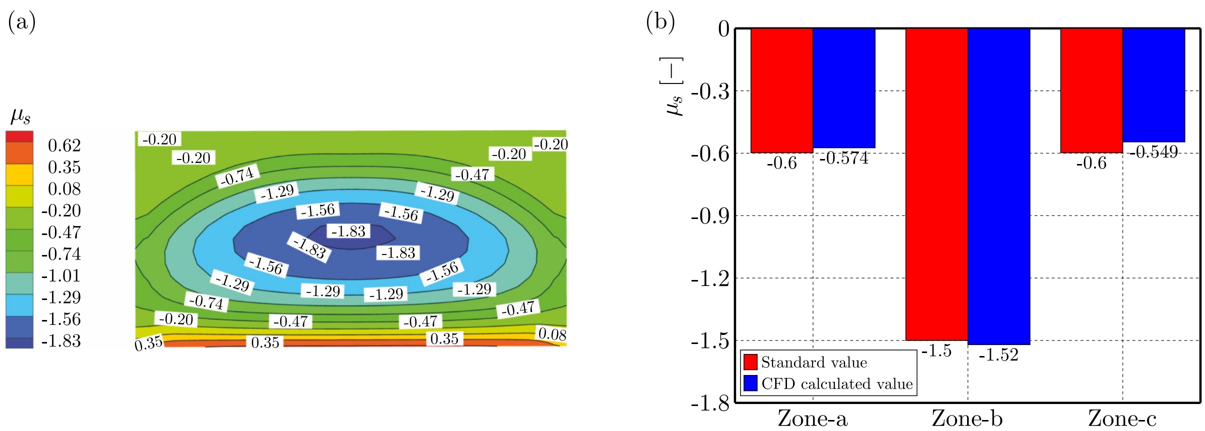


Fig. 9. (a) Local shape coefficient of arched roof; (b) mean shape coefficient of different zones.

It can be seen that under the above settings and the grid division, the deviation between the shape coefficient and the standard value is small, it indicates that the above settings and grid division are credible. In the following numerical simulation, the same settings, the grid division will be used.

## 3. Results and discussion

Based on codes (JGJ/T 481-2019, 2020), we selected 5 wind directions (0°, 45°, 90°, 135°, and 180°) for numerical simulation of the research object in this paper.

As shown in Fig. 10, the construction is divided into parts as shown in Fig. 10a, namely: peaks-A, B, C, D and trough-A, B, C. As shown in Fig. 10b, the model is divided into grids

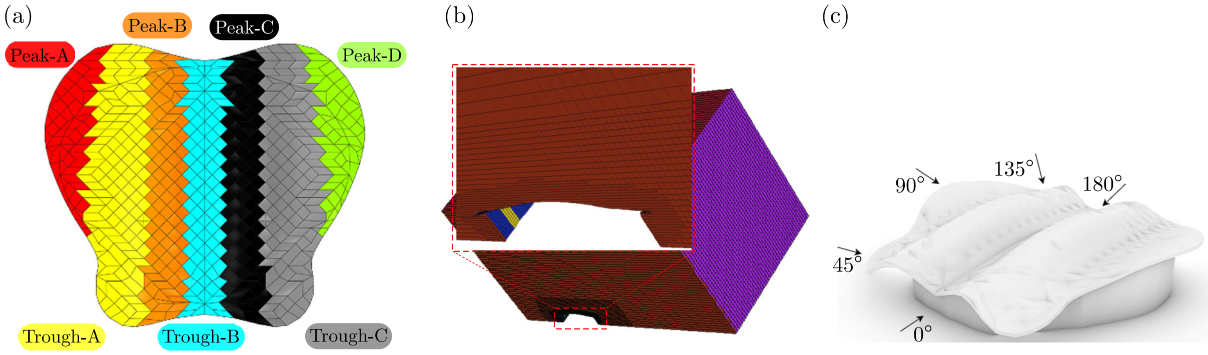


Fig. 10. (a) Roof zoning and naming; (b) grid area of roof and BOI; (c) wind directions.

according to the model in Grid 4. Measurement points are also set on the model roof before calculation. Table 5 lists the coordinates of roof measurement points. The setting of wind directions is shown in Fig. 10c. Coordinates of roof structure monitoring points (m).

Table 5. Coordinates of roof measurement points.

| Positions | Measuring point 1 | | | Measuring point 2 | | | Measuring point 3 | | | Measuring point 4 | | | Measuring point 5 | | |
|---|---|---|---|---|---|---|---|---|---|---|---|---|---|---|---|
| | $x$ | $y$ | $z$ | $x$ | $y$ | $z$ | $x$ | $y$ | $z$ | $x$ | $y$ | $z$ | $x$ | $y$ | $z$ |
| Peak-A | −36.45 | 63.54 | 17.93 | −43.19 | 43.44 | 16.33 | −36.18 | 29.51 | 17.73 | −42.17 | 10.91 | 17.33 | −40.82 | 3.75 | 17.52 |
| Trough-A | −26.43 | 68.87 | 9.89 | −28.45 | 45.44 | 12.34 | −26.68 | 20.26 | 12.18 | −13.22 | 11.37 | 11.31 | −15.49 | 2.89 | 10.52 |
| Peak-B | −14.28 | 69.13 | 17.22 | −15.24 | 48.97 | 16.15 | −13.59 | 31.03 | 16.08 | −13.22 | 11.37 | 17.57 | −14.49 | 2.89 | 16.92 |
| Trough-B | 0 | 67.35 | 10.52 | 0 | 52.63 | 12.07 | 0 | 31.73 | 9.64 | 0 | 11.37 | 8.72 | 0 | 2.89 | 9.92 |
| Peak-C | 14.28 | 69.13 | 17.14 | 15.24 | 48.97 | 16.28 | 13.59 | 31.03 | 16.07 | 13.22 | 11.37 | 17.45 | 14.49 | 2.89 | 17.02 |
| Trough-C | 26.43 | 69.13 | 9.88 | 27.66 | 45.77 | 12.16 | 27.5 | 20.2 | 12.13 | 13.22 | 11.37 | 11.31 | 15.49 | 2.89 | 10.52 |
| Peak-D | 36.45 | 63.54 | 17.93 | 43.19 | 43.44 | 16.33 | 36.18 | 29.51 | 17.73 | 42.17 | 10.91 | 17.33 | 40.82 | 3.75 | 17.52 |

### 3.1. Velocity and wind pressure distribution

As shown in Table 6, the peak velocity is the lowest under the 0° wind direction and the highest under the 45° wind direction. The maximum positive pressure occurs at the 90° wind directions and the maximum negative pressure occurs at the 45° wind direction.

Table 6. Velocity and pressure.

| Wind directions | Peak wind speed [m/s] | Peak maximum pressure [Pa] | Trough minimum pressure [Pa] |
|---|---|---|---|
| 0° | 13.93 | 9.63 | −120.77 |
| 45° | 18.36 | 19.96 | −228.13 |
| 90° | 15.91 | 75.33 | −65.13 |
| 135° | 16.17 | 46.72 | −120.77 |
| 180° | 13.85 | 35.53 | −77.48 |

Under the 0° wind direction, Figs. 11a and 11b show that the windward surface of the fence is first impacted by the incoming flow, which then quickly passes along the fence, reaching maximum velocity at the largest cross-section of the fence. Correspondingly, Figs. 11c and 11d show that there is a larger negative pressure at this location, indicating a transition from positive to negative pressure on the fence. In the vertical direction, as seen in Fig. 11b, the incoming flow does not undergo significant rotational disturbance on the roof due to the presence of

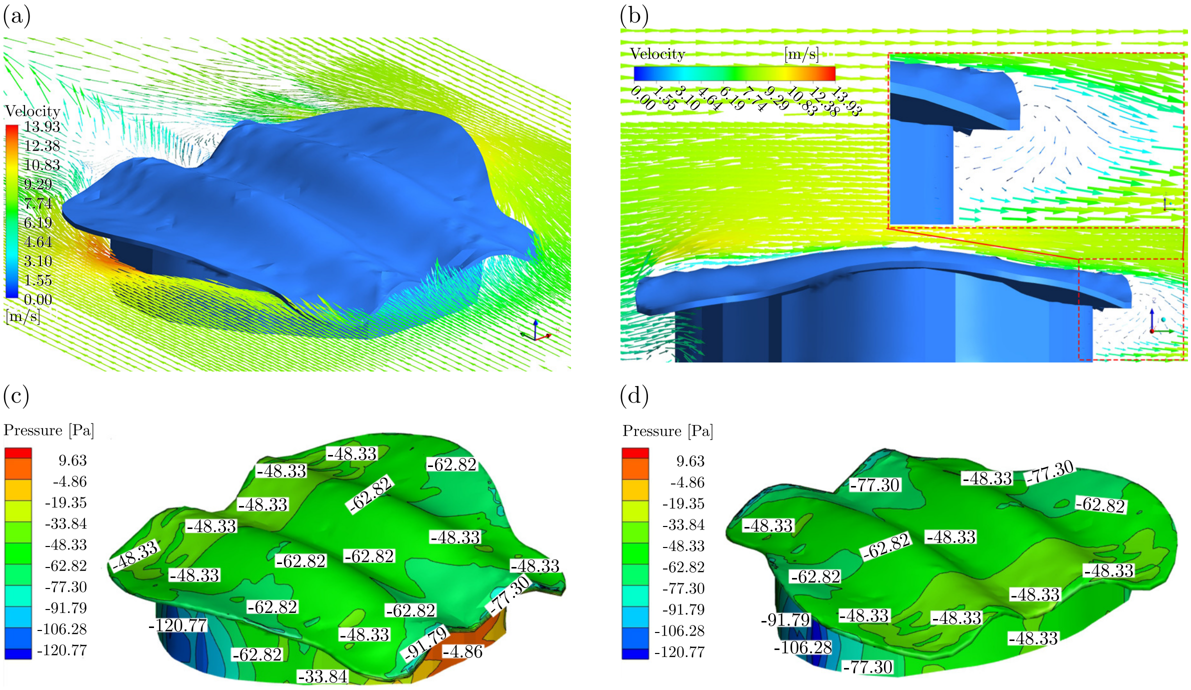


Fig. 11. (a)–(b) Velocity vector; (c)–(d) contours of wind pressure under 0° direction.

the variable cross-section arch roof, but instead rapidly moves towards the rear of the model along the direction of the incoming flow, effectively reducing the impact of the incoming flow and preventing strong airflow rotation at the roof tail, resulting in relatively smaller negative pressures.

Under the 45° wind direction, the interaction between the incoming flow and the building is significantly intensified. As shown in Fig. 12a, the disturbance of the incoming flow at the fence is greater compared to the 0° wind direction. Figure 12b shows that there are higher wind

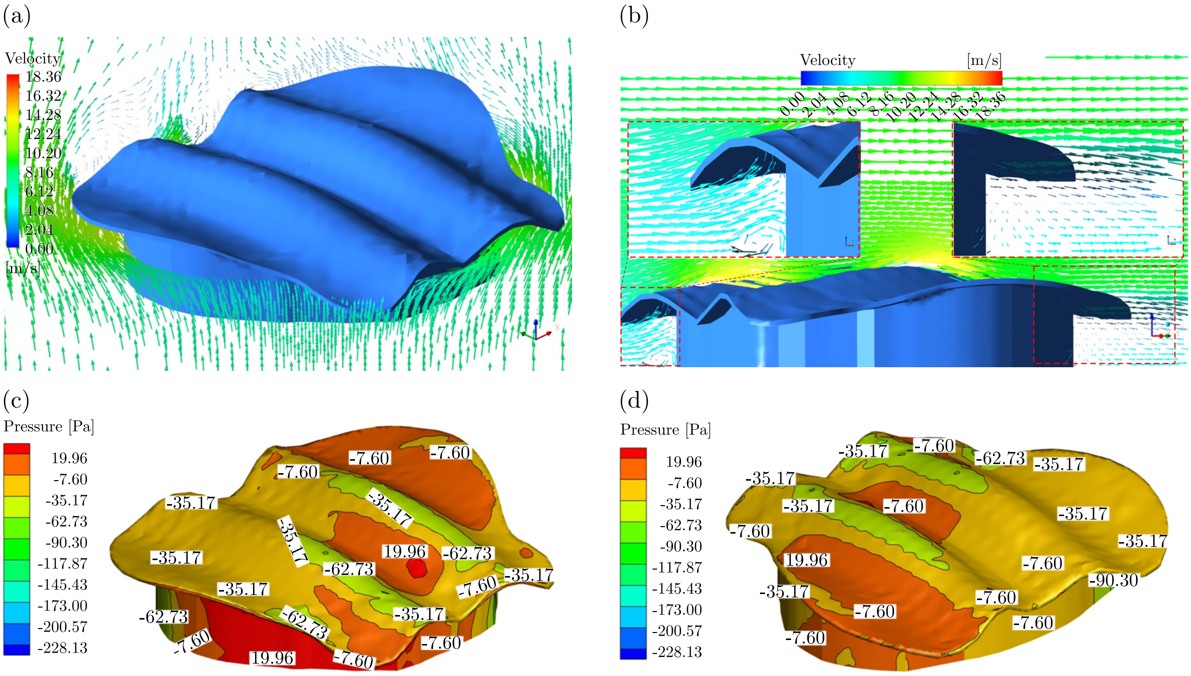


Fig. 12. (a)–(b) Velocity vector; (c)–(d) contours of wind pressure under 45° direction.

speeds at the peak-A and B of the roof since the incoming flow does not pass directly over the variable cross-section roof in the span direction but instead moves laterally through the wavy structure. Figures 12c and 12d indicate that there is a larger area of negative pressure at these locations. However, there is no significant airflow disturbance at peak-D and the trailing edge of the building after the impact of the airflow is weakened by peak-A, B, and trough-A. Comparing Figs. 12c and 12d, it can be observed that the suction force on the roof at peak-A, B, C, and D gradually decreases, and there is a region of positive pressure at trough B, indicating that the airflow changes over the roof are more complex under the 45° wind direction.

The 90° and 45° wind directions share similarities. Figures 13a and 13b reveal that there is a significant airflow rotation at trough-A and B under the 90° wind direction, with a larger rotation area at trough-A and a smaller one at trough-B. Figures 13c and 13d show that the strong impact also results in positive pressure in this area. While at trough-C, there is no significant airflow disturbance, and the flow quickly passes over the roof. The roof pressure under the 90° wind direction shows a large area of positive pressure, with relatively higher peak positive pressures. This is because the 90° wind direction represents the most distinct structural feature of the roof, causing the incoming flow to be most obstructed as it passes over the roof. Additionally, the larger positive pressures on the roof appear at the ends of the building, which is the result of the interaction between the flow fields near the fence and at the ends of the roof.

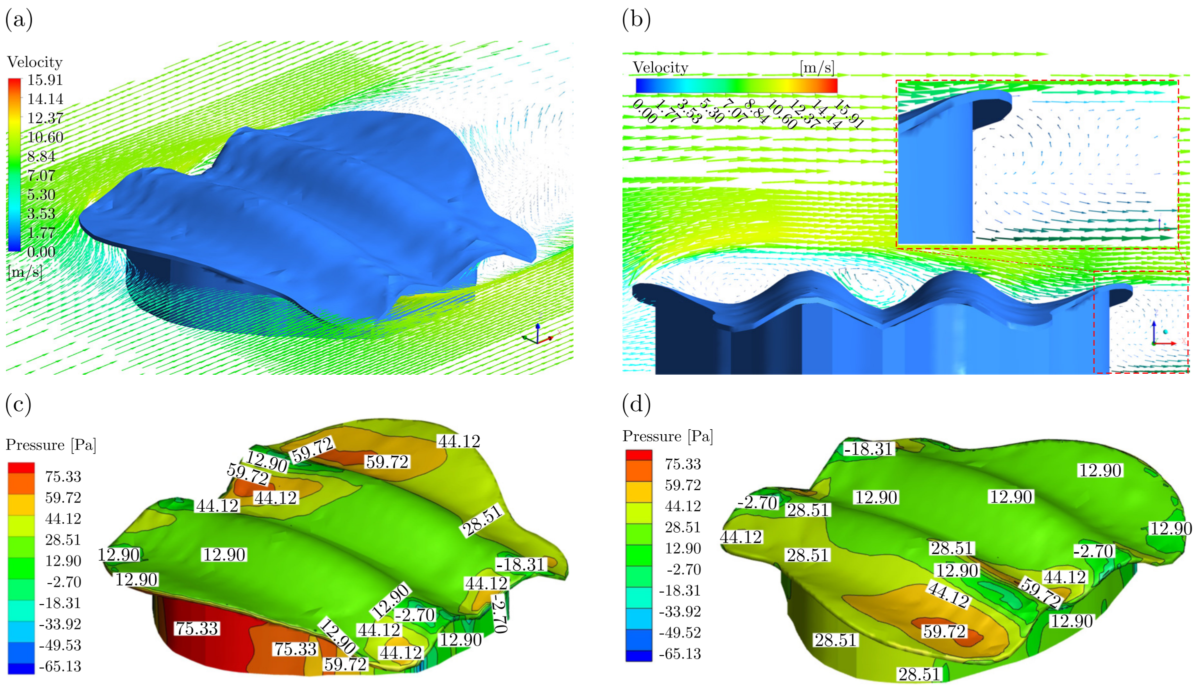


Fig. 13. (a)–(b) Velocity vector; (c)–(d) contours of wind pressure under 90° direction.

Under the 135° wind direction, the velocity changes around the roof are similar to those in a wind direction of 45°, with peak-A, B, and C mainly experiencing negative pressure, peak-D mainly experiencing positive pressure and all three troughs are mainly under positive pressure. As shown in Fig. 10a, the roof structure is narrower at the front and wider at the back. Therefore, under the 45° wind direction, the structural features along the direction of the incoming flow increase, the rise height of a roof is increasing continuedly, the obstruction to incoming flow is increasing. Conversely, under the 135° wind direction, the structural features decrease along the flow direction, resulting in decreasing obstruction. Thus, under the 45° wind direction, the roof experiences larger areas and values of negative pressure and smaller areas and values of positive pressure, while the opposite is true under the 135° wind direction.

The velocity situation under the 180° wind direction is similar to 0° wind direction, with little difference in the peak velocities and their locations. As previously analyzed, compared to the 0° wind direction where the roof width gradually increases, both the peak velocity and the suction force on the roof under the 180° wind direction are smaller than those under the 0° wind direction, due to the structural features of the building under the 180° wind direction gradually decreasing.

In summary, there will be significant changes in wind speed and roof pressure or the building will experience greater pressure when the incoming flow passes through the building, if the structural features of the building decrease. The results from Figs. 11 to 14 indicate that the flow fields near the ends of the building are more complex, showing more complex situations in the roof pressure. Additionally, the parts of the roof that first contact the incoming flow will experience greater suction or smaller pressure, and as the incoming flow develops, the suction gradually decreases or the pressure gradually increases.

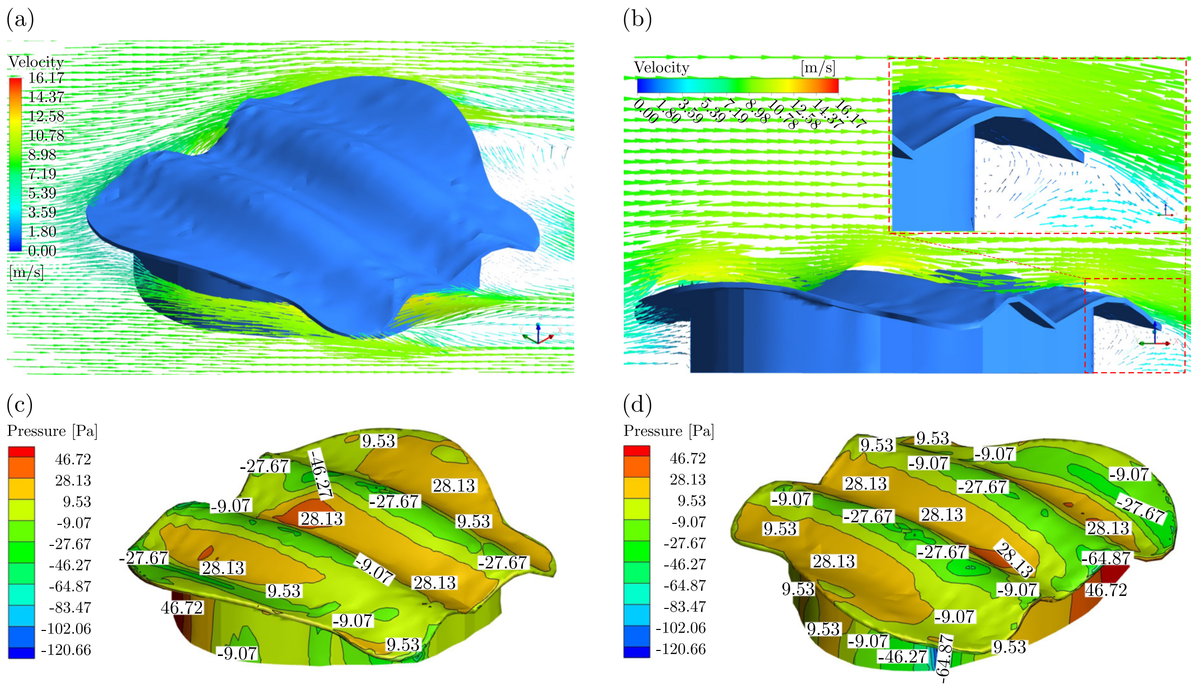


Fig. 14. (a)–(b) Velocity vector; (c)–(d) contours of wind pressure under 135° direction.

In Subsection 2.1 of this paper, it is mentioned that the building roof has actually a portion of the cantilevered structure. Wang *et al.* (2023) point out: "The size effect modifies the distribution of the pressure field within the columnar vortex at the leading edge of the windward side". It can be seen that the structural characteristics of the building play an important role in protecting the roof from the velocity vector diagram. As shown in Fig. 9, there will be rotation and vortices, and the disturbance of this part of the airflow will result in a large area of negative pressure at the top of the roof, ultimately affecting the distribution of the roof's shape coefficients after the incoming flow contacts the roof and the fence structure. The cantilevered structure of this building effectively weakens this phenomenon. From part (b) of Figs. 11–15, it can be seen that after the windward side contacts, the produced rotation and vortices are small, such as under the 0° and 180° directions, or vortices appear, but these vortices do not develop to affect the roof structure area, such as under the 90° and 45° wind directions due to the cantilevered structure. The wake region is also the same, where the wake rotation is limited under the cantilevered structure. Both structural characteristics and size effects affect the wind pressure characteristics of a building's roof, and the design structure of this building demonstrates good superiority.

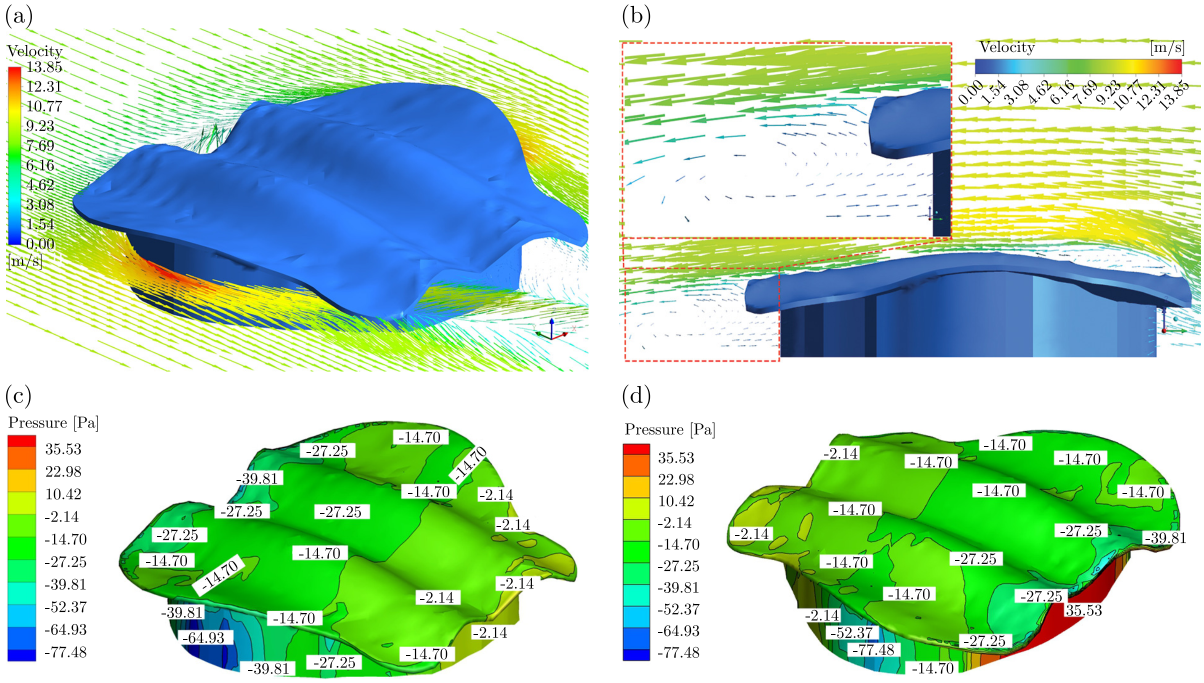

Fig. 15. (a)–(b) Velocity vector; (c)–(d) contours of wind pressure under 180° direction.

Blackmore and Tsokri (2006) imply that for arched roofs, "The suctions on the central roof zones are highly dependent on the position along the roof", which is fully confirmed in the research object of this paper. For example, as shown in Fig. 12c, a small area and small positive pressure appear in the region trough-B and the peak-C under the 45° wind direction. Subsequently, the pressure changes to a large area of negative pressure near the maximum rise height, and then as the rise height decreases, the negative pressure value on the roof increases, indicating that the suction force on the roof decreases. However, the pressure changes on the roof are more severe and are also more affected by adjacent roof structures in continuous-span buildings unlike single-span structures, which is different from the literature.

### 3.2. Wind pressure coefficient and mean shape coefficient

Based on the calculation results, wind pressure coefficients and mean shape coefficients for the building surface were calculated using Eq. (2.11), Eq. (2.12), and Eq. (2.13), respectively, and the results were visualized in contour maps. The results are presented in Table 7, Fig. 16, and Fig. 17.

Table 7. Mean shape coefficients.

| Zone | Wind directions | | | | |
|---|---|---|---|---|---|
| | 0° | 45° | 90° | 135° | 180° |
| Peak-A | −1.78621 | −0.94503 | 0.342702 | −0.70617 | −0.98657 |
| Trough-A | −2.19161 | −0.72146 | 0.639788 | 0.898425 | −1.38848 |
| Peak-B | −1.64519 | −1.26795 | 0.534423 | 0.649691 | −1.29938 |
| Trough-B | −1.96209 | −0.04145 | 1.105404 | 0.994864 | −1.35412 |
| Peak-C | −1.60694 | −1.36378 | 0.655461 | −0.623750 | −1.31092 |
| Trough-C | −2.16317 | −0.24185 | 1.142049 | 0.188102 | −1.37046 |
| Peak-D | −1.78401 | −0.23856 | 1.120191 | 0.238559 | −0.98535 |

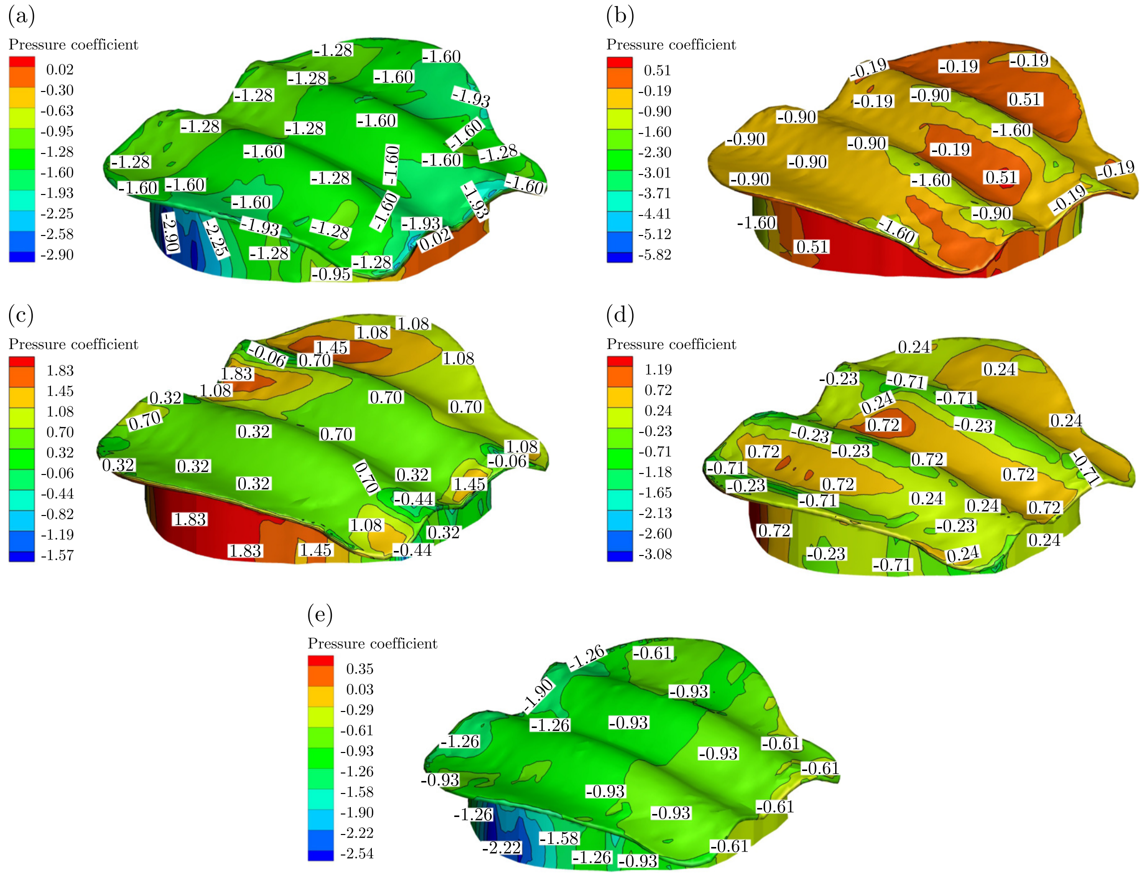


Fig. 16. Wind pressure coefficient of different wind directions: (a) 0°; (b) 45°; (c) 90°; (d) 135°; (e) 180°.

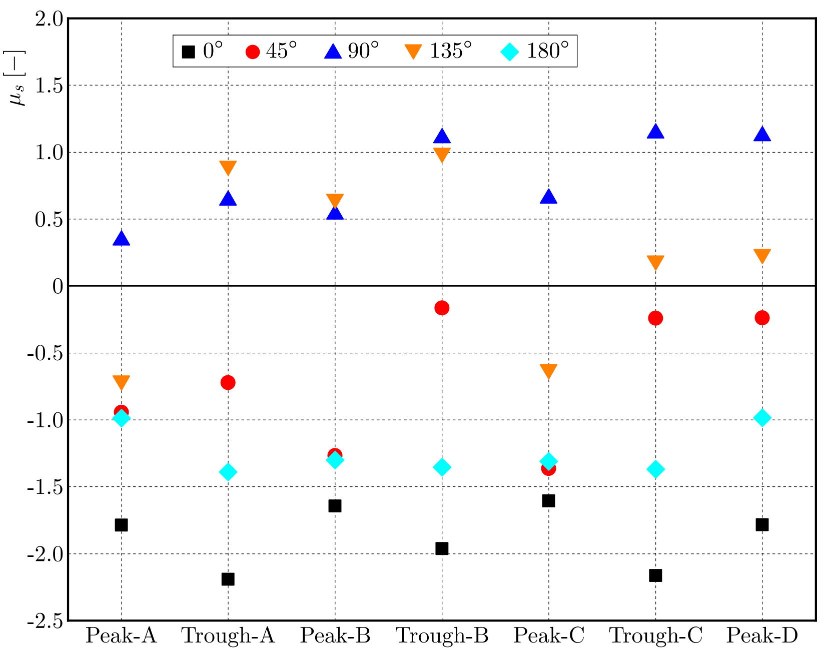


Fig. 17. Mean shape coefficient of roof area under different wind directions.

Both large positive and small negative wind pressure coefficients appeared at the cantilever structure of the roof among the five wind directions. For the roof structure, only under the 90° wind direction did a large area of positive wind pressure coefficients appear, while under the other wind directions, the roof wind pressure coefficients were mainly negative. These results indicate that the roof is mainly acted upon by suction, with the pressure acting mainly on the windward side of the roof cantilever.

From Table 7 and Fig. 17, it can be seen that the wind pressure coefficients are relatively stable under the 0° and 180° wind directions, with values distributed around −2.0 and −1.25, respectively. The shape coefficients under the 180° wind direction are greater than those under the 0° wind direction in all areas, indicating that the suction force on the roof under the 180° wind direction is less than that under the 0° condition. This is because under the 180° wind direction, the roof windward surface area is larger, receiving a greater impact from the incoming flow, and the building cantilever withstands a larger positive pressure, which also greatly weakens the incoming flow. The force on the roof also decreases after the incoming flow is weakened by the windward surface, resulting in a smaller suction force on the roof under the 180° wind direction, which corresponds to Figs. 16a and 16b.

As for the 45° and 135° wind directions, the shape coefficients have larger fluctuations, especially under the 135° wind direction, where the roof shape coefficients are more complex, with both positive and negative values. Specifically, under the 135° wind direction, Fig. 17 shows that in addition to the shape coefficients at peak-A and C being negative, the values of the shape coefficients in the other areas are all positive. Under the 45° wind direction, the fluctuations are slightly reduced, with the roof shape coefficients being negative and larger in value than under the 135° wind direction. This is because the suction force on the roof is relatively small.

It can be seen that under the 135° wind direction, the structural features of the roof decrease along the incoming flow direction, leading to a more complex flow field and changes in roof wind pressure and shape coefficients. Under the 45° wind direction, the structural features of the roof gradually increase, and the wavy roof plays a greater role in guiding the flow after the incoming flow passes through the windward side, resulting in larger wind pressure coefficients and shape coefficients at peak-D and trough-C.

There is a large area of positive wind pressure coefficients and shape coefficients under the 90° wind direction with only a small part of negative wind pressure coefficients at the ends of the roof structure, compared to other wind directions. Combining Fig. 13b, it can be seen that under the 90° wind direction, the building impedes the incoming flow to a greater extent, and there is a significant degree of rotation and disturbance when the wind flows perpendicular to the wavy roof, causing the roof to be acted upon by positive pressure. It is worth noting that although the impediment to the incoming flow is significant, the wavy roof structure causes the incoming flow to weaken rapidly, the roof does not receive a large positive pressure.

## 4. Conclusion

This paper focuses on a CFD simulation of a continuous-span building with a variable-section arch-shaped roof as the main structure, analyzing its flow field characteristics, wind pressure distribution, wind pressure coefficients, and shape coefficients under different wind directions. The findings provide guidance for the wind resistance design and subsequent safety maintenance of such buildings. The main conclusions are as follows:

1) Under different wind directions, the fence of building experiences significant positive pressures, the maximum negative pressure and maximum velocity appear at the transition points of the fence structure's cross-section under different directions. Except for the 90° wind direction, where the roof is primarily acted upon by positive pressure, the roof structure experiences a large area of negative pressure under other wind directions, which is due to the maximum obstruction of the wave-shaped structure of the roof being perpendicular to the wind direction.
2) Along the symmetric direction of the building under various wind directions, both the wind pressure coefficients and the mean shape coefficients tend to be evenly distributed.

Under oblique winds, i.e., at 45° and 135° wind directions, the wind pressure coefficients and mean shape coefficients on the roof change complexly, with smaller negative wind pressure coefficients appearing at the areas of the roof that firstly come into contact with the incoming flow, and some positive shape coefficients can also appear at the highest point of the roof's rise. Under the 90° wind direction the roof mainly experiences positive wind pressure coefficients, with positive shape coefficients, indicating that the roof is mainly acted upon by positive pressure.

3) The influence of structural characteristics and size effects is the most significant part of the results, mainly divided into two points: firstly, the cantilevered structure of the roof plays a weakening role on the incoming flow and wake diffusion, which can reduce the pressure on the roof. Secondly, the influence of size effect changes produced by the flow passing over the roof.

4) It is important to note that the above results require further verification through wind tunnel tests or on-site measurements. In future research, the authors will consider these two methods, which can provide a more comprehensive study of the building. Additionally, wind resistance design of structures includes the calculation of many important parameters; the authors hope to analyze these parameters in future calculations.

## References

1. Blackmore, P.A. & Tsokri, E. (2006). Wind loads on curved roofs. *Journal of Wind Engineering and Industrial Aerodynamics*, *94*(11), 833–844. https://doi.org/10.1016/j.jweia.2006.06.006

2. del Coz Díaz, J.J., García Nieto, P.J., Vilán Vilán, J.A., Alvarez Rabanal, F.P., Navarro-Manso, A., & Alonso-Martínez, M. (2013). Nonlinear analysis of the pressure field in industrial buildings with curved metallic roofs due to the wind effect by FEM. *Applied Mathematics and Computation*, *221*, 202–213. https://doi.org/10.1016/j.amc.2013.06.067

3. Esfeh, M.K., Sohankar, A., Shahsavari, A.R., Rastan, M.R., Ghodrat, M., & Nili, M. (2021). Experimental and numerical evaluation of wind-driven natural ventilation of a curved roof for various wind angles. *Building and Environment*, *205*, Article 108275. https://doi.org/10.1016/j.buildenv.2021.108275

4. GB 50009-2012 (2012). *Load code for the design of building structures.* China Architecture & Building Press.

5. JGJ/T 481-2019 (2020). *Standard for wind loads on roof structures.* Ministry of Housing and Urban-Rural Development of the People's Republic of China, Beijing.

6. Kim, R., Lee, I., Yeo, U., & Lee, S. (2019). Estimating the wind pressure coefficient for single-span greenhouses using an large eddy simulation turbulence model. *Biosystems Engineering*, *188*, 114–135. https://doi.org/10.1016/j.biosystemseng.2019.10.009

7. Li, F., Ni, Z., & Shen, S. (2007). Characteristics of wind pressure on typical roofs under different terrain conditions (in Chinese). *Journal of Building Structures*, *28*(1), 119–124. https://doi.org/10.14006/j.jzjgxb.2007.01.017

8. Li, Y., Hu, W., & Wang, L. (2010). State-of-art: wind tunnel investigation on wind pressure distribution of large-span spatial structures with typical shapes (in Chinese). *Acta Aerodynamica Sinica*, *28*(1), 32–38.

9. Li, Y., Yukio, T., & Shen, Z. (2006). Wind tunnel test for wind pressure distribution characteristics of cylindrical shells (in Chinese). *Journal of Tongji University (Natural Science)*, *34*, 1457–1464.

10. Ma, R. & He, M. (2006). Discussion on concept design of long span special steel roof structures (in Chinese). *Journal of Building Structures*, *27*(4), 61–64. https://doi.org/10.14006/j.jzjgxb.2006.04.009

11. Meng, F.Q., He, B.J., Zhu, J., Zhao, D.X., Darko, A., & Zhao, Z.Q. (2018). Sensitivity analysis of wind pressure coefficients on CAARC standard tall buildings in CFD simulations. *Journal of Building Engineering*, *16*, 146–158. https://doi.org/10.1016/j.jobe.2018.01.004

12. Pagnini, L., Torre, S., Freda, A., & Piccardo, G. (2022). Wind pressure measurements on a vaulted canopy roof. *Journal of Wind Engineering and Industrial Aerodynamics*, *223*, Article 104934. https://doi.org/10.1016/j.jweia.2022.104934

13. Paluch, M.J., Loredo-Souza, A.M., & Blessmann, J. (2003). Wind loads on attached canopies and their effect on the pressure distribution over arch-roof industrial buildings. *Journal of Wind Engineering and Industrial Aerodynamics*, *91*(8), 975–994. https://doi.org/10.1016/S0167-6105(03)00047-3

14. Sun, W. & Zhang, Q. (2020). Universal equivalent static wind loads of fluctuating wind loads on large-span roofs based on compensation of structural frequencies and modes. *Structures*, *26*, 92–104. https://doi.org/10.1016/j.istruc.2020.04.008

15. Tian, Y., Guan, H., Shao, S., & Yang, Q. (2021). Provisions and comparison of Chinese wind load standard for roof components and cladding. *Structures*, *33*, 2587–2598. https://doi.org/10.1016/j.istruc.2021.06.011

16. Wang, Y., Liu, H., Lei, M., Chen, Z., Tse, T.K.T., Li, C.Y., & Fu, Y. (2023). Aerodynamic analysis of an ultra-long and ultra-wide industrial building under wind loading: Insights into flow dynamics and pressure distribution characteristics. *Journal of Building Engineering*, *76*, Article 107144. https://doi.org/10.1016/j.jobe.2023.107144

17. Zhang, G., Zhang, Q., Fan, F., & Shen, S. (2021). Numerical simulations of snowdrift characteristics on multi-span arch roofs. *Journal of Wind Engineering and Industrial Aerodynamics*, *212*, Article 104593. https://doi.org/10.1016/j.jweia.2021.104593

*Manuscript received May 10, 2024; accepted for publication January 22, 2025;*
*published online April 5, 2025.*